ARTICLE   OPEN

Check for updates

Thiol-based defect healing of WSe$_2$ and WS$_2$

Aviv Schwarz[1,2,13], Hadas Alon-Yehezkel [2,3,4,13], Adi Levi[2,4], Rajesh Kumar Yadav[2,4], Koushik Majhi[2,4], Yael Tzuriel[2,4], Lauren Hoang[5], Connor S. Bailey [5], Thomas Brumme[6,7], Andrew J. Mannix[8], Hagai Cohen[9], Eilam Yalon [10], Thomas Heine [7], Eric Pop [5,8,11], Ori Cheshnovsky[1,12] and Doron Naveh[2,4✉]

Recent research on two-dimensional (2D) transition metal dichalcogenides (TMDCs) has led to remarkable discoveries of fundamental phenomena and to device applications with technological potential. Large-scale TMDCs grown by chemical vapor deposition (CVD) are now available at continuously improving quality, but native defects and natural degradation in these materials still present significant challenges. Spectral hysteresis in gate-biased photoluminescence (PL) measurements of WSe$_2$ further revealed long-term trapping issues of charge carriers in intrinsic defect states. To address these issues, we apply here a two-step treatment with organic molecules, demonstrating the "healing" of native defects in CVD-grown WSe$_2$ and WS$_2$ by substituting atomic sulfur into chalcogen vacancies. We uncover that the adsorption of thiols provides only partial defect passivation, even for high adsorption quality, and that thiol adsorption is fundamentally limited in eliminating charge traps. However, as soon as the molecular backbone is trimmed and atomic sulfur is released to the crystal, both bonds of the sulfur are recruited to passivate the divalent defect and the semiconductor quality improves drastically. Time-dependent X-ray photoelectron spectroscopy (XPS) is applied here together with other methods for the characterization of defects, their healing, leading energies and occupation. First-principles calculations support a unified picture of the electronic passivation of sulfur-healed WSe$_2$ and WS$_2$. This work provides a simple and efficient method for improving the quality of 2D semiconductors and has the potential to impact device performance even after natural degradation.

INTRODUCTION

The flurry of activity in two-dimensional (2D) semiconductors over the last decade has resulted in rapid advancement toward electronic and optoelectronic applications[1,2]. Among the most prominent materials of this class are transition metal dichalcogenide (TMDC) semiconductors that hold great promise for future technologies, including low-power electronics[3], radio frequency (RF) electronics[4], optoelectronics[2] and more. The existing gaps for achieving the technological maturity of these materials are the growth of large-scale high-quality materials[2], the development of efficient doping methods[5], and finally, processes for achieving low-impedance metallization and interfaces[6].

Chemical vapor deposition (CVD) is considered among the most promising synthetic methods for achieving large-scale TMDC monolayers. Advances in CVD growth of monolayer TMDCs allow for large area coverage by polycrystalline WSe$_2$ and MoS$_2$[7,8], as well as the formation of lateral heterojunctions of MoSe$_2$/WSe$_2$ and vertical heterojunctions[9], bandgap-engineered alloys of W$_x$Mo$_{(1−x)}$S$_{2(1−y)}$Se$_{2y}$[10] and more. However, the quality of CVD-grown materials has not yet reached maturity, and therefore the crystals often contain imperfections and defects. The most common defects of CVD-grown layers are chalcogen atom vacancies[11,12] and oxidation[13,14]. Such defects and their influence on the electronic[15] and optical[16] properties are being extensively studied[17]. Defects are usually probed by analytical techniques,

including X-ray photoelectron spectroscopy (XPS), that can associate the defects with composition and elemental oxidation states[18], photoluminescence spectroscopy of sub-bandgap emissions[19] and Raman spectroscopy, where peak widths are correlated to the defect densities via anharmonic contributions of crystalline imperfections[20].

While growth methods continuously progress toward improved crystalline quality, post-growth improvements and "healing" processes propose faster progress in this field. Several defect healing methods have been demonstrated thus far, including an almost perfect healing driven by migration of sulfur into selenium vacancies in MoS$_2$/MoSe$_2$/MoS$_2$ heterostructures[21], defect passivation by thiol healing agents[22] and by adsorption of metal-organic molecular agents[23]. In this work, we studied the defects of CVD-grown monolayer WSe$_2$ and developed a passivation method that reduces their density. Our strategy for defect healing is based on three steps: (1) desorption of oxygen from Se vacancy sites ("activation" of vacancy), (2) thiol adsorption at active vacancy sites, and finally, (3) thermal annealing that drives sulfur injection into chalcogen vacancy sites. We show that the adsorption of thiol molecules on activated WSe$_2$ exchanges the oxide defects with shallow defects associated with the single-valent molecules. Significant reduction in defect densities is achieved by annealing the molecularly coated crystals and releasing atomic sulfur into the crystal.

[1]Department of Chemistry, Tel Aviv University, Tel Aviv 6997801, Israel. [2]Faculty of Engineering, Bar-Ilan University, Ramat-Gan 52900, Israel. [3]Department of Chemistry, Bar-Ilan University, Ramat-Gan 52900, Israel. [4]Bar-Ilan Institute for Nanotechnology and Advanced Materials, Ramat-Gan 52900, Israel. [5]Department of Electrical Engineering, Stanford University, Stanford, CA 94305, USA. [6]Wilhelm-Ostwald-Institute of Physical and Theoretical Chemistry, Leipzig University, Linnéstr. 2, D-04103 Leipzig, Germany. [7]Theoretical Chemistry, TU Dresden, Mommsenstr. 13, 01062 Dresden, and Helmholtz-Center Dresden-Rossendorf. Institute of Resource Ecology, Leipzig Research Branch, Permoserstr. 15, 04318 Leipzig, Germany. [8]Department of Materials Science & Engineering, Stanford, CA 94305, USA. [9]Department of Chemical Research Support, Weizmann Institute of Science, Rehovot 76100, Israel. [10]Andrew and Erna Viterbi Faculty of Electrical Engineering, Technion - Israel Institute of Technology, Haifa 320003, Israel. [11]Precourt Institute for Energy, Stanford University, Stanford, CA 94305, USA. [12]Institute of Light-Matter Interactions, Tel Aviv University, Tel Aviv 6997801, Israel. [13]These authors contributed equally: Aviv Schwarz, Hadas Alon-Yehezkel. ✉email: doron.naveh@biu.ac.il
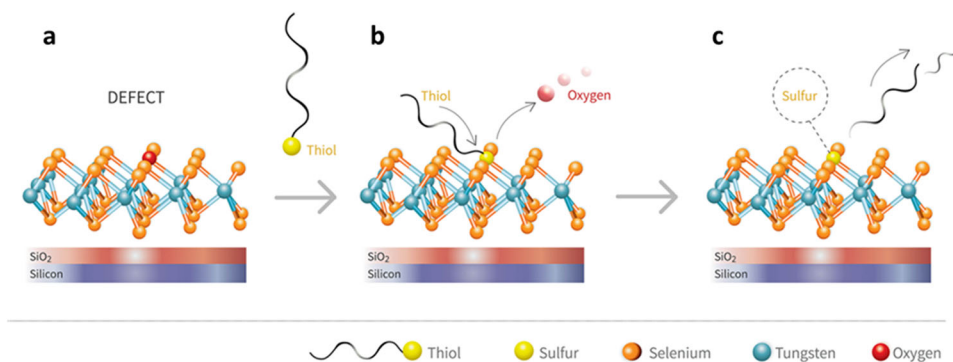
Fig. 1 A schematic illustration of the WSe₂ monolayer treatments used in this work. a A bare WSe$_2$ crystal with a single Se vacancy, here occupied by an adsorbed O atom. **b** Thiolated WSe$_2$, where the thiol is anchored on the Se vacancy sites. **c** Annealed samples with sulfur atom substitution at the locations of the original Se vacancy sites.
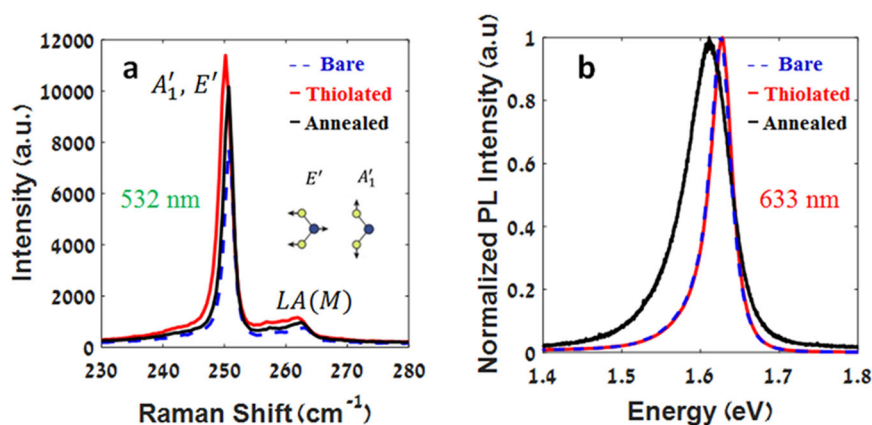
Fig. 2 Raman and photoluminescence of WSe₂ measured at room temperature. a Raman and **b** normalized PL spectra of bare (dash blue), thiol coated (red line) and annealed coated (black line) monolayer WSe$_2$. The laser wavelength used in each measurement is indicated as 532 nm and 633 nm, respectively.

RESULTS AND DISCUSSION

Defect healing process

Figure 1 depicts the schematics of defects and healing after thiol treatments on CVD-grown WSe$_2$[24]. WSe$_2$ crystals were grown by CVD on SiO$_2$/Si substrates (see "Methods") and then kept at ambient conditions for 4 months before their defect density was assessed. These spontaneously oxidized samples were the starting point of this work and are considered here as "bare" (Fig. 1a) WSe$_2$ samples. We employed surface passivation by a gentle (see "Methods" section for details) thermal annealing followed by a thiol dipping treatment, rinsing and drying. These types of samples are referred to as "thiolated" (Fig. 1b). Finally, thiolated samples (Fig. 1c) were subjected to a more aggressive annealing process, and this sample type is referred to as "annealed" samples. For more details on the chemical processes, see the "Methods" section.

### Characterization of bare, thiolated and annealed samples

Long-range order of the WSe$_2$ samples before and after chemical treatment was inferred by Raman spectroscopy, as shown in Fig. 2a. For all WSe$_2$ samples, the Raman peaks at ~260 and ~263 cm^{-1} correspond to the overtone of the longitudinal acoustic (LA) phonon branch, and to a phonon of the A-symmetric optical branch, both at the M point[25], having the same amplitude ratio to the A'_1 and E' peaks at ~250 cm^{-1}. Since the LA(M) mode is associated with crystalline disorder[26], we deduce that the long-range order, as measured by Raman spectroscopy, is not affected by the chemical processes[26]. Despite the lower mass and stronger

spring constant of S relative to Se, we observe no shifts or broadening in the A'_1 and E' modes at ~250 cm^{-1}—indicating that the concentration of sulfur is too low to leave a spectral signature. In contrast, the electronic structure was strongly affected by these substitutional sites, as verified by photoluminescence (PL), Fig. 2b.

Room temperature PL spectra of the bare (blue line) and thiolated (red line) samples reveal a characteristic peak at 1.64 eV corresponding to the optical bandgap (A exciton) of monolayer WSe$_2$[27]. However, the annealed sample signal (black line) is broadened, red-shifted and strongly reduced in height. Such effects reflect the modified electronic structure; see below the low-temperature data.

Attribution of gate-modulated PL to defect states

By applying gate-voltage bias during PL measurements (see Supplementary Fig. 4) of monolayer WSe$_2$ samples, we observed a transient modulation of the PL signal in response to the voltage. Upon continuous gate-voltage modulation of the PL, a hysteresis curve in the PL peak energy, spectral width, and peak intensity (Fig. 3a–c, respectively) was recorded for both exfoliated and CVD-grown monolayer WSe$_2$. To elucidate the nature of the hysteresis, the PL spectrum was continuously measured in response to each gate-voltage step. Transients on the time scale of 100 s were observed, where the PL gradually returned to its previous steady-state values. The results for PL peak energy, spectral width and peak intensity after a gate-voltage step of $\Delta V = 10V$ (at $t = 0$) are shown in Fig. 3d–f, respectively. The transient behavior is well
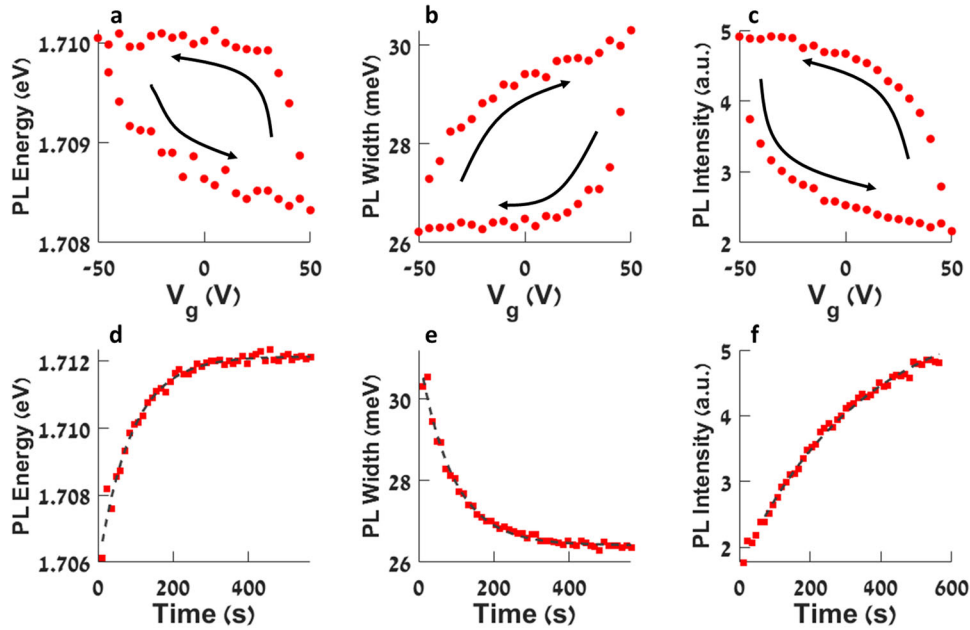
Fig. 3 Hysteresis curves in gate-modulated photoluminescence. a Modulation of PL peak energy. **b** Modulation of PL peak width. **c** Modulation of the PL peak intensity. **d–f** Evolution of the PL emission in response to a 10 V gate-voltage step: PL peak energy, spectral width and peak intensity (respectively) vs. time.
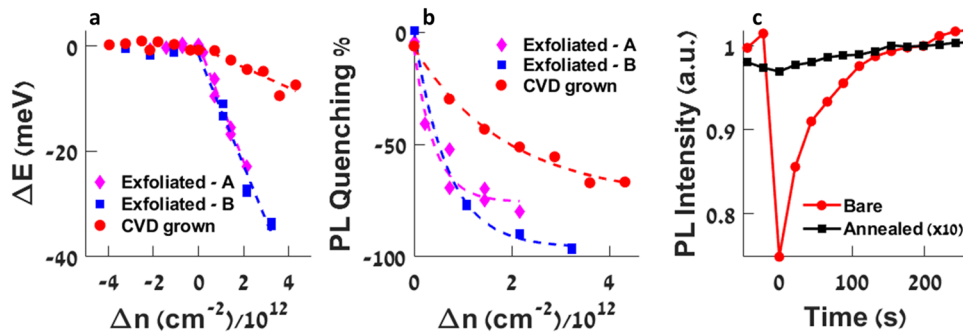
Fig. 4 Gate-modulated photoluminescence. a PL energy shift and **b** PL intensity quenching of exfoliated (pink diamonds, blue rectangles) monolayer flakes and of CVD-grown (red dots) samples. **c** Effect of the defect healing process on the transient in PL intensity.

described by an exponent function

$$y = (y_f - y_0)\left(1 - e^{-\frac{t}{\tau}}\right),\qquad(1)$$

as shown in Fig. 3d–f by the dash black marking.

The change in carrier density Δn in response to the voltage step ΔV corresponds to the capacitance of our devices (285 nm SiO_2/Si) by $\triangle n = C \cdot \triangle V \cdot q^{-1}$, where $C = 1.2 \cdot 10^{-8} Fcm^{-2}$ and q is the electron charge. By modulating the voltage step, the relation of Δn to the PL is resolved for the peak energy and for the quenching of the PL amplitude, as described in Fig. 4a, b.

Figure 4a shows that positive charge (negative Δn) causes no significant change in the PL energy, while negative charge results in a spectral redshift. Figure 4b displays the voltage-mediated intensity quenching of the PL in exfoliated (pink diamonds, blue rectangles) and CVD-grown WSe_2 (red dots). These two features may be understood as a process where field-effect injection of electrons charges some defect states near the valence band edge, thus preventing thermal generation in the adjacent valence levels through Pauli blocking (Supplementary Fig. 5). At the same time, photoexcitation of these trapped charges occurs, further reducing the ratio of available radiative recombination paths. This leads to photorecombination into higher energy valence levels and non-radiative recombination into uncharged defect levels, resulting in

Table 1. The lower bound estimation of defect density n_d in WSe_2 for different devices using data from Fig. 4b.	
Device	$n_d (cm^{-2})$
Exfoliated A	$1.3 \cdot 10^{12}$
Exfoliated B	$2.1 \cdot 10^{12}$
CVD grown	$6.0 \cdot 10^{12}$

spectral broadening, spectral redshift and quenched intensity in the observed PL spectra. The results shown in Supplementary Figs. 6 and 7 support this optical trapping/detrapping model and describe its dependence on the optical generation and temperature, respectively. Interestingly, the redshift in exfoliated devices A and B follows the same trend, while the slope of the CVD-grown device is about 5 times smaller, indicating a larger density of defect states by the same factor. The quenching of the PL signal (Fig. 4b) is proportional to the population of field-effect injected electrons. Eventually, it reaches saturation which depends on the density of defect states. The lower bound of defect density (Table 1) is evaluated as corresponding to the saturation point in the PL quenching, such as in Fig. 4b (here taken as 99% of signal

Table 2. XPS-derived binding energies (BE) and atomic concentrations (AC) of selected elements, including calculated Se/W and S/W ratios.

		W^{Se}	W^{ox}	Se^W	Se^{ox}	W^{ox}/W^{Se}	Se^{ox}/Se^W	Se^{tot}/W^{tot}	S/W^a (%)
Bare	BE (eV)	33.3	34.33	55.57	56.5–57.6				
	AC (%)	0.04	0.06	0.09	0.16	1.50	1.78	2.09	
Thiolated	BE (eV)	33.43	36.47	55.67	56.5				
	AC (%)	0.34	0.03	0.63	0.03	0.09	0.05	1.83	<25
Annealed	BE (eV)	33.20	35.90–36.11	55.44	56.22				
	AC (%)	0.605	0.053	1.12	0.16	0.09	0.14	1.89	<19
Fluorinated	BE (eV)	32.2	32.8	54.38	54.86				
	AC (%)	0.47	0.05	0.87	0.15	0.11	0.17	1.96	~3.5[b]

The complete compositional analysis and XPS spectra of Se 3d and W 4f are given in the Supplementary Information (Supplementary Table S1, Supplementary Fig. S1). Here W^{Se} is the XPS signal of W bounded to Se; W^{ox} is the oxidized tungsten, Se^W is the selenium bounded to tungsten fraction; Se^{tot}/W^{tot} is the ratio of the total (oxidized and non-oxidized) Se signal to the total W signal and S/W is the ratio of sulfur to the total signal of W.
[a]Upper limit values are for the density of S atoms per surface W sites, as deduced from the maximal signal that may be associated with S in the (noisy) spectra. Relative errors are 50%.
[b]S/W ratio is calculated by assuming: (1) no loss of F atoms (namely 17 per molecule) and (2) by averaging over sample thickness. Uncertainty of ±15% (relative error) should be considered due to variations in the crystal thickness.

minimal value). This estimation yields a ratio of x5 in the defect density of CVD-grown samples relative to exfoliated samples and is in agreement with the results from Fig. 4a.

Figure 4c shows the gate-modulated PL intensity before (red dots) and after (black rectangles) the defect healing process. The lack of PL transient and hysteresis in defect-healed samples shows that the PL quenching is caused by other reasons, not associated with defects. This quenching was also observed in low-temperature measurements of Fig. 7, and in both cases, the signal drop is within one order of magnitude.

Chemical effects of the defect healing process
The chemical nature of these modifications was examined by X-ray photoelectron spectroscopy (XPS). Table 2 provides the WSe₂ composition, showing clearly the effectiveness of chemical treatments. Mainly, oxidation that is very apparent in the bare crystals is largely removed upon thiolation. The line-shapes of measured W 4f and Se 3d signals (W^{tot} and Se^{tot}, respectively) were deconvoluted into contributions of oxidized tungsten (W^{ox}) and oxidized selenium (Se^{ox}) and the well-resolved signals of the host WSe₂, labeled as W^{Se} and Se^W for the selenium-bounded tungsten and tungsten-bounded selenium, respectively, both obeying the expected chemical shifts (see Supplementary Information).

The XPS-derived compositions (Table 2) indicate that upon thiolation, oxidation of the WSe₂ is drastically reduced. An independent observation that the thiols are spatially located on the chemically reduced WSe₂ was obtained by Time-of-Flight secondary ion mass spectrometry (ToF-SIMS) maps, as depicted in Fig. 5. This provides direct proof for the success of thiol adsorption on WSe₂[28]. Fig. 5a displays a ToF-SIMS mapping of thiolated WSe₂ crystals on the SiO₂/Si surface, showing the lateral distribution of Se⁻, WO₃⁻ and Si⁻ (from the substrate) mass fractions. The spatial distribution of the WSSe⁻ mass fraction is depicted in Fig. 5b, showing an almost perfect overlap with the shape of the crystal in Fig. 5a, indicating that the signals of thiols and sulfur indeed originate in molecules adsorbed on WSe₂ (see also Supplementary Fig. 3).

Figure 5c shows XPS sulfur signals in representative spectra recorded from the thiolated (top) and annealed (bottom) samples. Despite a technical difficulty due to overlap with intense Se signals, two experimentally weak (yet significant and repeatable) S 2p doublets were resolved, providing further proof for the existence of thiol molecules on the surface. Curve fitting of these spectra encounters significant flexibility, and the S-concentration

values in Table 2 stand for the limit of *maximal* intensity that can be associated with sulfur. The binding energies of the S 2p doublets, with the characteristic split of 1.18 eV in each, correspond to two sulfur states, from which we quantified the effect of corresponding defect healing treatments. Independently, reference experiments suggest that thiol adsorption directly on the SiO₂ substrate is of very low efficiency. Hence, the measured amounts of molecules are directly associated with adsorption on the WSe₂ crystals.

The estimated surface densities of adsorbed sulfur in Table 2, expressed as S/W ratios, suggest considerable surface coverage by the sulfur species, both for the thiolated and the annealed samples. Combined with the S 2p binding energies (Fig. 5c), we conclude that the adsorption of thiols involves chemical bonding that is sufficiently robust to withstand the annealing process and the effective removal of the thiol molecular backbone. Note that the Se/W ratio (Table 2) is lower for the thiolated and annealed samples (relative to the bare one), indicating that the pre-deposition thermal treatment of high-vacuum heating (see "Methods" section) increases the number of Se vacancies and enables subsequent anchoring of the thiol molecules.

As an additional test of thiol adsorption efficiency, we repeated the experiment with molecules consisting of a fluorinated backbone, such that the quantification of adsorption could gain from the detection of fluorine signals. Results are given in Table 2 and in Supplementary Table 1, for which our coverage estimation assumes no degradation in the molecules (namely, a 17:1 ratio between F and S), yielding S/W ~3.5%. The effective thickness obtained in this case, about 2–3 Å only, corresponds to the lower limit of (yet within reasonable agreement with) densities obtained for the CH backbones, which means for both systems that molecules are far from being compactly arranged. It should be noted, however, that adsorption efficiency and packaging may be affected by the nature of the backbone and, therefore, direct comparison with the hydrogenated backbones may be misleading.

In addition to the compositional analysis, using very delicate scan conditions (see Supplementary Information), the XPS peak positions were exploited to gain insights into energy level variations in the WSe₂ crystals. In particular, the W 4f doublets in Fig. 6a, before and after treatment, exhibit peak shifts that reflect a 220 meV difference in the Fermi level. This Fermi level shift is a result of the chemical treatment. Accordingly, a Se 3p line shift of 250 meV is measured, in good agreement with the tungsten data. As described in detail below, our experimental
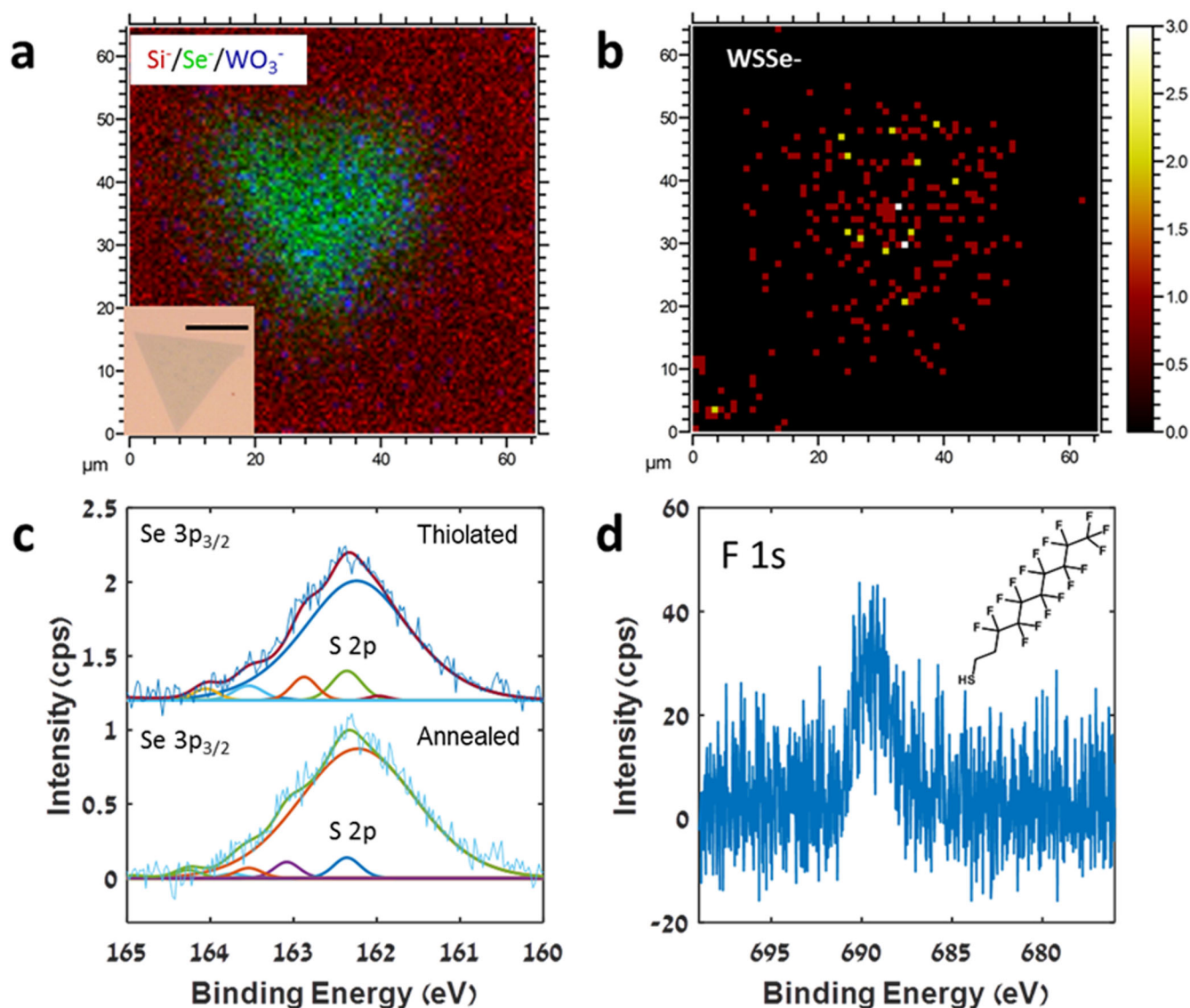
Fig. 5 Measurements of thiol sulfur density. a ToF-SIMS mapping of Si^- (red), Se^- (green) and WO_3^- (blue) mass fragments of the sample. Insert: an optical microscope image (50 X) of WSe_2 crystal. **b** A ToF-SIMS map depicting the lateral distribution of $WSSe^-$ counts that overlap with the decanthiol-coated crystal of (**a**). **c** The XPS Se $3p_{3/2}$ window in the (top) thiolated sample; (bottom) annealed sample. Signal height is normalized here to unity, and the energy scale of the thiolated sample was shifted by 0.325 eV, such as to visually align the Se peak positions of the two samples. Note the two tiny doublets associated with S 2p signals. **d** The XPS F 1 s core level in a sample thiolated with PFDT molecules.

protocol is aimed at a careful elimination of the *beam-induced* (X-ray) effects, and the presented data are believed to account faithfully, within 20 meV, for the zero exposure limit (see additional details in Supplementary Fig. 1).

Next, we present the *beam-induced* shifts at very early stages of exposure to the X-ray source (Fig. 6b), given as a function of exposure time. Since the X-ray radiation leads to loss of electrons, upon finite sample conductivity peaks are expected to gradually shift to higher binding energies (BEs), a trivial result of positive charging inherent to XPS. Here, the bare sample (Fig. 6b blue line) presents *negative* peak shifts (to *lower* BEs), while the thiolated (red line) samples have very small peak shifts, and the annealed sample (black line) manifests positive peak shifts. Each of the measured shift values is corrected for the Si line shifts because the electrostatic potential at the WSe_2 crystals floats on that of the silica underneath. Raw line shift values are given in Supplementary Fig. 2. Interestingly, the net shift values that reflect charging at

individual WSe_2 islands reveal marked qualitative differences between the samples.

By recording the sample's back contact current, we verified that positive current was maintained in all cases, corresponding integrally to positive charge accumulation. Hence the emergence of negative-like charging reflects electron capturing preferentially at the surface. This means that the bare WSe_2 crystals consist of relatively large electron trap concentrations, presumably deep states that retain long lifetimes for the trapped electrons. Upon low-dose exposures to the X-ray, occupation of these traps is increased with time and abnormal shifts emerge. However, prolonged exposures would eventually saturate these traps and thus terminate the progress of the observed effect, as indeed found experimentally.

The accumulation of space-charge within WSe_2 crystals results from hot charges generated by the X-ray irradiation and the availability of charge traps in the material (see Supplementary Information). We infer that hot-electron injection from the silica to
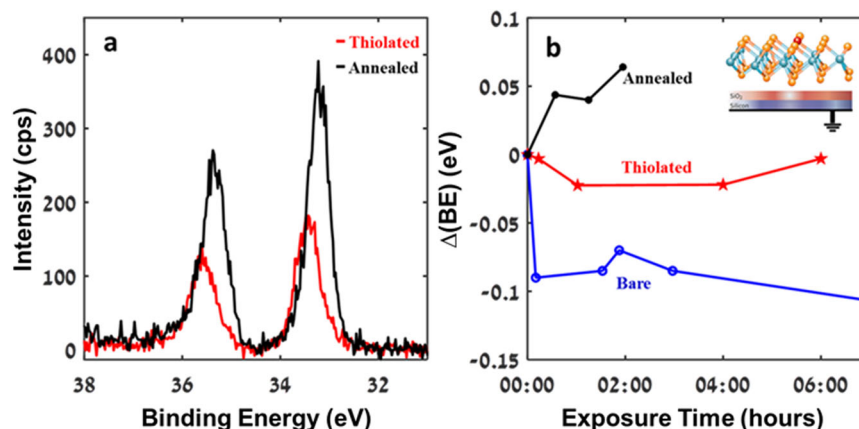
Fig. 6 Assessment of doping effects by XPS. a The XPS W 4f doublet in thiolated samples before (red line) and after (black line) annealing. A peak shift by 220 meV to lower binding energies is obtained after annealing. **b** The time-dependent X-irradiation-induced binding-energy shifts, Δ(BE), of the W line (the component associated with WSe$_2$) for the three samples, all evaluated in reference to the shifts in the substrate-Si line, such as to exclusively express the TMD- potential variations. Inset: the measurement configuration of the grounded sample.

an empty electron trap within the WSe$_2$ yields a net difference between line-shifts of W (and Se), compared to Si, as summarized graphically in Fig. 6b (see Supplementary Information for the details of referencing to the Si core level shifts). Obviously, passivation of deep electron traps would suppress the effect of negative-like charging, as indeed demonstrated by the two treatments studied here: the adsorption of thiols and, even more, the subsequent annealing. Consequently, obtaining 'normal' positive charging is a qualitative indication for successful passivation of the majority of deep electron traps in our WSe$_2$ samples.

Low-temperature PL measurements of treated and untreated samples

The electronic modification of the chemically treated WSe$_2$ was further investigated by low-temperature PL measurements (at 100 K) as summarized in Fig. 7a. Before annealing, in both (bare and thiolated) samples, the exciton peak appears at ~1.69 eV[29], and after annealing the exciton peak appears at 1.67 eV (Fig. 7b–d, respectively).

In bare (oxidized) WSe$_2$ (Fig. 7b), we identify both positive (X^+) and negative (X^-) trion states at energies of 1.68 eV and 1.63 eV, respectively, in addition to an emission peak at 1.53 eV (D) that may be associated with defects[30,31]. In the molecularly coated sample (Fig. 7c), a sharp peak (X^b) is observed at ~1.59 eV. It is associated with a bound exciton[15], next to the single-valent sulfur of the thiol that is bound to the carbon chain[32–34]. Notably, the negative trion has vanished. After annealing, the peak at 1.59 eV of the thiolated sample (Fig. 7d) vanishes, indicating that the thermal annealing trimmed the thiol molecule and released the sulfur to become a constituent of the WSe$_2$ crystal. We additionally performed an identical defect healing process on CVD-grown monolayer WS$_2$ flakes. The exciton PL peak at 1.9 eV of the annealed WS$_2$ sample has increased intensity and reduced spectral width compared to the bare sample (Fig. 7e). The intensity of the defect-related peak at 1.7 eV is reduced as well. Spectrally narrower exciton peaks and lower intensity defect peaks were observed in several flakes, as shown in Fig. 7f. In contrast, the exciton peak of the annealed sample is damped and broadened due to deformation of the conduction band and an indirect bandgap being induced by the sulfur passivation. This observation supports the XPS finding of an upward shift of the Fermi energy after sample annealing. Thus, we infer that the PL data agree well with the XPS results, showing that oxide-related electron traps were removed by the reaction with thiols. In annealed WSe$_2$, the observed broadening and reduced intensity of the PL signal may

be associated with the modified electronic structure of S-doped WSe$_2$, as explained below.

Electronic-structure calculations

To gain theoretical insight into the band structure modification due to sulfur substitutional passivation, we perform density-functional theory (DFT) calculations (for details, see "Methods"). We compare the computed band structure of WSe$_2$ with 2% Se vacancy (black line) to that of the same material with S substituting these defects (dashed red) in Fig. 8. Indeed, we infer from the calculation that molecular thiols (green dash, Fig. 8) can only partially passivate the selenium vacancy and that a complete release of atomic sulfur into the crystal (red dash, Fig. 8) results in efficient passivation that removes mid-gap states associated with Se vacancies. In addition, in the sulfur-passivated samples, the smallest interband transition is indirect, supporting the observed PL quenching and broadening of the annealed sample (Fig. 7a). This provides a unifying understanding of our experimental observations as to the chemical origin of defect states and their physical properties and influence on the semiconductor properties.

METHODS

Decanthiol (Sigma Aldrich CAS# 112-55-0) and 1H,1H,2H,2H-Perfluorodecanethiol (PFDT) (Sigma Aldrich CAS# 34143-74-3) were used as received. Polycrystalline, predominantly monolayer WSe$_2$ samples were grown directly on SiO$_2$/Si by chemical vapor deposition (CVD) using solid sources of Se powder (99.99% purity, Sigma Aldrich) and WO$_3$ powder (99.995% purity, Sigma Aldrich), at 900 °C as previously discussed in literature[35]. Perylene-3,4,9,10 tetracarboxylic acid tetrapotassium salt (PTAS) was used as a seeding promotor after treatment with hexamethyldisilazane (HMDS) to maximize the usable growth area on chip.

Thiol molecular deposition process

WSe$_2$ samples as-grown by CVD on SiO$_2$ (90-100 nm) on Si substrates were heated at high vacuum (10^{-6} Torr) for 1 h at 250 °C and then were immersed in a solution of Decanthiol (8 mM or 100 mM) in dry methanol for 72 h at room temperature (RT). The samples were washed with methanol and isopropanol, blow-dried with nitrogen and baked at low vacuum (10 mTorr, 10 sccm N$_2$) at 100 °C for 30 min. Finally, the samples were immersed in hot methanol (40 °C) overnight and washed with methanol and isopropanol and blow-dried with nitrogen.
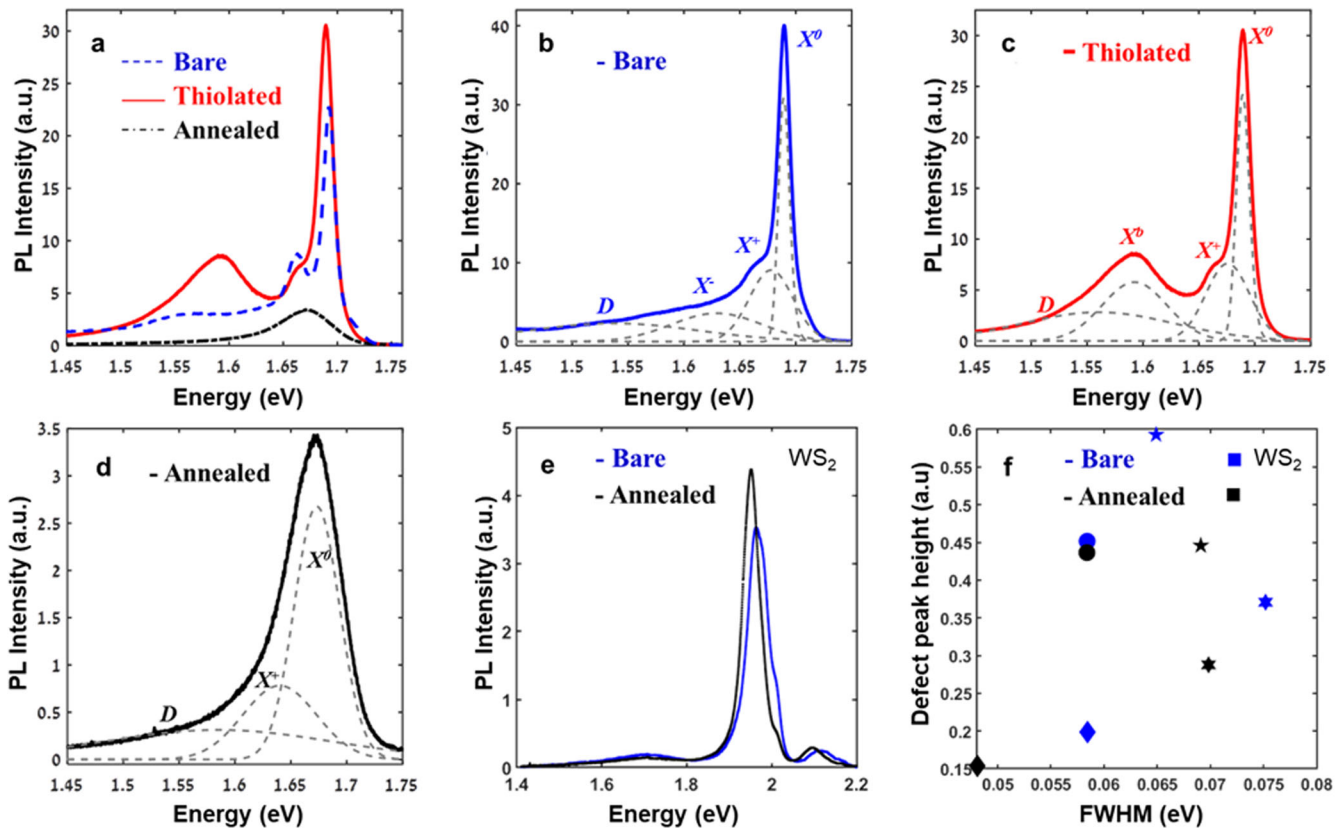
Fig. 7 The effects of thiol defect healing on photoluminescence spectra. a Combined spectra of WSe$_2$, **b** bare WSe$_2$, **c** thiolated WSe2, and **d** annealed WSe$_2$. **e** Photoluminescence spectra of bare and annealed WS$_2$. **f** Scatter plot of defect peak height *vs*. FWHM of exciton peak for bare and annealed WS$_2$ samples. Markers of the same shape indicate the same flake before and after the defect healing process. All spectra were measured at 100 K. WSe$_2$ and WS$_2$ samples were measured using 633 nm and 532 nm lasers, respectively.
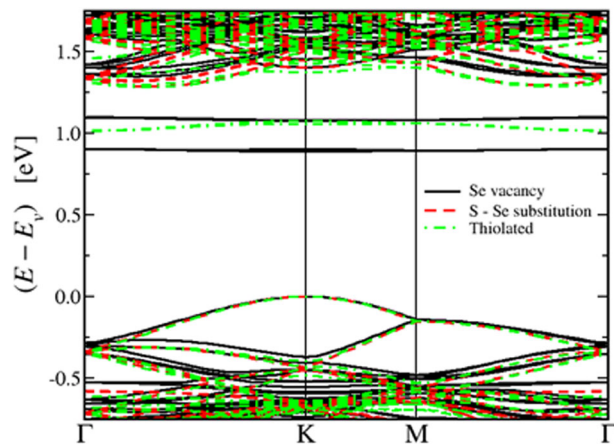
Fig. 8 Calculated electronic structure of monolayer WSe$_2$ before, during and after the defect healing process. The band structure with Se vacancy (black) is contrasted with WSe$_2$ with S substitution of Se vacancy sites (red, dashed line), showing the defect states of the vacancy and its passivation by sulfur. The bandgap becomes indirect after passivation. All band structures are aligned to the former valence-band maximum at the K point—the defect states in the bandgap are empty and partially filled for the "Se vacancy" and Thiolated systems, respectively.

Rapid thermal annealing process

Samples were heated to 500 °C for 3 min and remained at 500 °C for 10 min under 100 sccm nitrogen.

X-ray photoelectron spectroscopy (XPS)

Measurements were performed on a Kratos AXIS-Ultra DLD spectrometer, using mostly low power of the monochromatic Al Kα source, 15 W, and detection pass energies of 20–80 eV at an analysis area of ~0.5 mm in diameter. Beam-induced defects and damage creation during the measurement were carefully inspected via repeated scans on fixed spots and their comparison to fresh spot data. It should be noted in this respect that the concentration of WSe$_2$ crystals was varied on a mm scale, hence their coverage parameter had to be considered in the analyses.

As an integral part of the experiment, in situ work function measurements were repeatedly taken, such as to get an independent follow-up of electrostatic changes taking place in the sample under exposure to the X-ray beam. Standard methods for energy scale calibration were therefore of limited relevance, and the data presented here corresponds in all cases to raw measured binding energies. In turn, our data propose clear advantages in gaining electrical information, as indeed demonstrated in this study.

Raman and photoluminescence (PL) spectroscopy

WSe$_2$ crystals were measured in vacuum (~10 Torr) at temperatures of 100 K and 300 K (HFS600E-PB4, Linkam Scientific Instruments). Raman and PL spectra were acquired using a Raman microscope (LabRAM HR Evolution, HORIBA Scientific) with a 532 nm or 633 nm laser wavelength, as indicated in the text. Data were fit to an exponential broadened Gaussian using the Matlab peakfit function.

Time-of-flight secondary ion mass spectrometry (TOF-SIMS)

Time of flight secondary ion mass spectrometry (ToF-SIMS, ION-TOF GmbH TOF.SIMS 5) spectra images were taken using 25 keV Bi+ analysis ions (incident at 45°). Only negative ions were measured. In spectra mode, the mass resolution is 0.01 atomic mass units, and the lateral resolution is ~10 μm; in image mode, the lateral resolution is ~1 μm, but the mass resolution decreases dramatically.

Computational methods

All electronic-structure calculations have been performed within the framework of density-functional theory (DFT) as implemented in the Quantum ESPRESSO package[36,37], which uses a plane-wave basis set to describe the valence-electron wave functions and charge density. We employed full-relativistic, projector-augmented wave potentials[38]. We chose the Perdew-Burke-Ernzerhof functional[39] for the exchange-correlation energy and furthermore included dispersion corrections[40]. A cutoff of 55 and 500 Ry (1 Ry ~ 13.6 eV) for the wave functions and the charge density, respectively, has been used. The convergence has been checked with higher cutoffs, which lead to negligible changes in the relaxed structure and only slight shifts of the semi-core states. The Brillouin zone integration of the 5×5 supercell has been performed with a 4×4 Monkhorst-Pack grid[41] together with a Gaussian broadening of 0.005 Ry. The self-consistent solution of the Kohn-Sham equations was obtained when the total energy changed by less than 10^{-8} Ry and the maximum force on all atoms was less than 10^{-3} Ry a_0^{-1} ($a_0 \sim 0.529177$ Å is the Bohr radius). We furthermore used the 2D Coulomb cutoff technique as implemented in Quantum ESPRESSO[42]. The thiolated samples have been simulated by replacing a single Se atom with an ethanethiol radical (CH_3-CH_2-S). The band structures have been aligned to the former valence-band maximum of WSe_2—in the thiolated system, the defect states in the former bandgap are occupied, while they are empty in the systems with the Se vacancy.

DATA AVAILABILITY
Data are available on request from the authors.

REFERENCES
1. Fiori, G. et al. Electronics based on two-dimensional materials. *Nat. Nanotechnol.* **9**, 768 (2014).
2. Wang, Q. H., Kalantar-Zadeh, K., Kis, A., Coleman, J. N. & Strano, M. S. Electronics and optoelectronics of two-dimensional transition metal dichalcogenides. *Nat. Nanotechnol.* **7**, 699 (2012).
3. Ge, R. et al. Atomristor: nonvolatile resistance switching in atomic sheets of transition metal dichalcogenides. *Nano Lett.* **18**, 434–441 (2018).
4. Krasnozhon, D., Lembke, D., Nyffeler, C., Leblebici, Y. & Kis, A. MoS₂ transistors operating at gigahertz frequencies. *Nano Lett.* **14**, 5905–5911 (2014).
5. Cai, L. et al. Rapid flame synthesis of atomically thin MoO₃ down to monolayer thickness for effective hole doping of WSe2. *Nano Lett.* **17**, 3854–3861 (2017).
6. Allain, A., Kang, J., Banerjee, K. & Kis, A. Electrical contacts to two-dimensional semiconductors. *Nat. Mater.* **14**, 1195 (2015).
7. Smithe, K. K. H., English, C. D., Suryavanshi, S. V. & Pop, E. Intrinsic electrical transport and performance projections of synthetic monolayer MoS₂ devices. *2D Mater.* **4**, 011009 (2016).
8. Huang, J.-K. et al. Large-area synthesis of highly crystalline WSe₂ monolayers and device applications. *ACS Nano* **8**, 923–930 (2014).
9. Dong, R. & Kuljanishvili, I. Review Article: Progress in fabrication of transition metal dichalcogenides heterostructure systems. *J. Vac. Sci. Technol. B* **35**, 030803 (2017).
10. Xie, L. M. Two-dimensional transition metal dichalcogenide alloys: preparation, characterization and applications. *Nanoscale* **7**, 18392–18401 (2015).
11. Zhou, W. et al. Intrinsic structural defects in monolayer molybdenum disulfide. *Nano Lett.* **13**, 2615–2622 (2013).
12. Carozo, V. et al. Optical identification of sulfur vacancies: bound excitons at the edges of monolayer tungsten disulfide. *Sci. Adv.* **3**, e1602813 (2017).
13. Lin, Y.-C. et al. Revealing the atomic defects of WS₂ governing its distinct optical emissions. *Adv. Funct. Mater.* **28**, 1704210 (2018).
14. Nan, H. et al. Strong photoluminescence enhancement of MoS₂ through defect engineering and oxygen bonding. *ACS Nano* **8**, 5738–5745 (2014).
15. Wu, Z. et al. Defects as a factor limiting carrier mobility in WSe₂: a spectroscopic investigation. *Nano Res.* **9**, 3622–3631 (2016).
16. Tongay, S. et al. Defects activated photoluminescence in two-dimensional semiconductors: interplay between bound, charged, and free excitons. *Sci. Rep.* **3**, 2657 (2013).
17. Chen, Y. et al. Tuning electronic structure of single layer MoS₂ through defect and interface engineering. *ACS Nano* **12**, 2569–2579 (2018).
18. Islam, M. R. et al. Tuning the electrical property via defect engineering of single layer MoS₂ by oxygen plasma. *Nanoscale* **6**, 10033–10039 (2014).
19. Wu, Z. et al. Defect activated photoluminescence in WSe₂ monolayer. *J. Phys. Chem. C* **121**, 12294–12299 (2017).
20. Mignuzzi, S. et al. Effect of disorder on Raman scattering of single-layer MoS₂. *Phys. Rev. B* **91**, 195411 (2015).
21. Surrente, A. et al. Defect healing and charge transfer-mediated valley polarization in MoS₂/MoSe₂/MoS₂ trilayer van der Waals heterostructures. *Nano Lett.* **17**, 4130–4136 (2017).
22. Yu, Z. et al. Towards intrinsic charge transport in monolayer molybdenum disulfide by defect and interface engineering. *Nat. Commun.* **5**, 5290 (2014).
23. Ahn, H. et al. Efficient defect healing of transition metal dichalcogenides by metallophthalocyanine. *ACS Appl. Mater. Interfaces* **10**, 29145–29152 (2018).
24. Chen, J. et al. Plasmon-resonant enhancement of photocatalysis on monolayer WSe₂. *ACS Photonics* **6**, 787–792 (2019).
25. del Corro, E. et al. Excited excitonic states in 1L, 2L, 3L, and bulk WSe₂ observed by resonant Raman spectroscopy. *ACS Nano* **8**, 9629–9635 (2014).
26. Wu, Z. & Ni, Z. Spectroscopic investigation of defects in two-dimensional materials. *Nanophotonics* **6**, 1219–1237 (2017).
27. Yan, T., Qiao, X., Liu, X., Tan, P. & Zhang, X. Photoluminescence properties and exciton dynamics in monolayer WSe₂. *Appl. Phys. Lett.* **105**, 101901 (2014).
28. Chou, H., Ismach, A., Ghosh, R., Ruoff, R. S. & Dolocan, A. Revealing the planar chemistry of two-dimensional heterostructures at the atomic level. *Nat. Commun.* **6**, 7482 (2015).
29. Ross, J. S. et al. Electrically tunable excitonic light-emitting diodes based on monolayer WSe₂ p–n junctions. *Nat. Nanotechnol.* **9**, 268 (2014).
30. Zhao, W. et al. Origin of indirect optical transitions in few-layer MoS₂, WS₂, and WSe₂. *Nano Lett.* **13**, 5627–5634 (2013).
31. Yin, J. et al. Large-area highly crystalline WSe₂ atomic layers for ultrafast pulsed lasers. *Opt. Express* **25**, 30020–30031 (2017).
32. Lin, T. et al. Site-selective photoluminescence in thiol-capped gold nanoclusters. *Appl. Phys. Lett.* **100**, 103102 (2012).
33. Pham, V. P. & Yeom, G. Y. Recent advances in doping of molybdenum disulfide: industrial applications and future prospects. *Adv. Mater.* **28**, 9024–9059 (2016).
34. Schoenfisch, M. H. & Pemberton, J. E. Air stability of alkanethiol self-assembled monolayers on silver and gold surfaces. *J. Am. Chem. Soc.* **120**, 4502–4513 (1998).
35. Liu, Z., Hou, W., Pavaskar, P., Aykol, M. & Cronin, S. B. Plasmon resonant enhancement of photocatalytic water splitting under visible illumination. *Nano Lett.* **11**, 1111–1116 (2011).
36. Giannozzi, P. et al. QUANTUM ESPRESSO: a modular and open-source software project for quantum simulations of materials. *J. Phys. Condens. Matter* **21**, 395502 (2009).
37. Giannozzi, P. et al. Advanced capabilities for materials modelling with Quantum ESPRESSO. *J. Phys. Condens. Matter* **29**, 465901 (2017).
38. Blöchl, P. E. Projector augmented-wave method. *Phys. Rev. B* **50**, 17953 (1994).
39. Perdew, J. P., Burke, K. & Ernzerhof, M. Generalized gradient approximation made simple. *Phys. Rev. Lett.* **77**, 3865 (1996).
40. Grimme, S., Antony, J., Ehrlich, S. & Krieg, H. A consistent and accurate ab initio parametrization of density functional dispersion correction (DFT-D) for the 94 elements H-Pu. *J. Chem. Phys.* **132**, 154104 (2010).
41. Monkhorst, H. J. & Pack, J. D. Special points for Brillouin-zone integrations. *Phys. Rev. B* **13**, 5188 (1976).
42. Sohier, T., Calandra, M. & Mauri, F. Density functional perturbation theory for gated two-dimensional heterostructures: theoretical developments and application to flexural phonons in graphene. *Phys. Rev. B* **96**, 075448 (2017).

ACKNOWLEDGEMENTS

AUTHOR CONTRIBUTIONS
A.S., A.L., R.K.Y., H.A., S.B., L.H., A.J.M., E.Y., E.P., O.C. and D.N. prepared and processed samples. H.A., H.C., A.S., O.C. and A.L. measured and analyzed samples. T.H. and T.B. performed calculations and theoretical analysis. All authors discussed the results and agreed to the content of the manuscript.

COMPETING INTERESTS
The authors declare no competing interests.

ADDITIONAL INFORMATION
Supplementary information The online version contains supplementary material available at https://doi.org/10.1038/s41699-023-00421-0.

Correspondence and requests for materials should be addressed to Doron Naveh.

Reprints and permission information is available at http://www.nature.com/reprints

Publisher's note Springer Nature remains neutral with regard to jurisdictional claims in published maps and institutional affiliations.

Supplementary Materials for:

Thiol-Based Defect Healing of WSe₂ and WS₂

Aviv Schwarz, [†,1,2] Hadas Alon-Yehezkel, [†,2,3,4] Adi Levi,[2,4] Rajesh Kumar Yadav,[2,4] Koushik Majhi,[2,4] Yael Tzuriel,[2,4] Lauren Hoang,[5] Connor S. Bailey,[5] Thomas Brumme,[6,7] Andrew J. Mannix,[8] Hagai Cohen,[9] Eilam Yalon,[10] Thomas Heine,[7] Eric Pop,[5,8,11] Ori Cheshnovsky[1,12] and Doron Naveh[2,4,*]

1 Department of Chemistry, Tel Aviv University, Tel Aviv 6997801, Israel

2 Faculty of Engineering, Bar-Ilan University, Ramat-Gan 52900, Israel

3 Department of Chemistry, Bar-Ilan University, Ramat-Gan 52900, Israel

4 Bar-Ilan Institute for Nanotechnology and Advanced Materials, Ramat-Gan 52900, Israel

5 Department of Electrical Engineering, Stanford University, Stanford, CA, 94305, USA

6 Wilhelm-Ostwald-Institute of Physical and Theoretical Chemistry, Leipzig University, Linnéstr. 2, D-04103 Leipzig, Germany

7 Theoretical Chemistry, TU Dresden, Mommsenstr. 13, 01062 Dresden, and Helmholtz-Center Dresden-Rossendorf. Institute of Resource Ecology, Leipzig Research Branch, Permoserstr. 15, 04318 Leipzig, Germany

8 Department of Materials Science & Engineering, Stanford CA 94305, USA

9 Department of Chemical Research Support, Weizmann Institute of Science, Rehovot 76100, Israel

10 Andrew and Erna Viterbi Faculty of Electrical Engineering, Technion - Israel Institute of Technology, Haifa 320003, Israel

11 Precourt Institute for Energy, Stanford University, Stanford, CA 94305, USA

12 Institute of Light-Matter Interactions, Tel-Aviv University, Tel-Aviv 6997801, Israel

† These authors contributed equally

* email: doron.naveh@biu.ac.il

Keywords: TMDC, Defect, Vacancies, Photoluminescence, Defect Metrology

Supplementary Note I: XPS Analysis and Calibration

Composition analysis by XPS:

Supplementary Table 1. Binding energy (BE) and atomic concentration (AC) data for the relevant elements in the examined samples: The total W 4f and Se 3p signals (W^{tot} and Se^{tot}, respectively), the oxidized tungsten (W^{ox}) and oxidized selenium (Se^{ox}), the *clean* tungsten selenide signals including selenium-bounded tungsten (W^{Se}) and tungsten-bounded selenium (Se^W). the fully oxidized Si (SiO_2, Si^{ox}), sub-oxide Si (SiO_{2-x}, Si^{sub}), oxygen (O) and carbon (C). Calculated Se/W ratios, surface coverage by the WSe_2 flakes and Sulfur percentages in the coated samples are given as well.

		W^{Se}	W^{ox}	Se^W	Se^{ox}	Si^{Ox}	Si^{sub}	O	C	Se^{tot}/W^{tot}	S/W (%) ±50%[1]
bare	BE (eV)	33.3	34.33	55.57	56.5-57.6	104.32	102.33	533.76	285.33		
	AC (%)	0.04	0.06	0.09	0.16	29.43	1.23	62.33	6.66	2.09	
thiolated	BE (eV)	33.43	36.47	55.67	56.5	104.3	102.33	533.75	285.4		
	AC (%)	0.34	0.03	0.63	0.03	28.85	0.7	60.55	8.84	1.83	< 25
annealed	BE (eV)	33.20	35.90-36.11	55.44	56.22	104.2	102.25	533.67	285.25		
	AC (%)	0.605	0.053	1.12	0.16	29.57	0.65	61.98	5.86	1.89	< 19
fluorinated	BE (eV)	32.2	32.8	54.38	54.86	104.2	102.02	533	284.72		
	AC (%)	0.47	0.05	0.87	0.15	26.7	0.47	57.15	8.6	1.96	~ 3.5[2]

[1] Upper limit values are for the density of S atoms per surface W sites, as deduced from the *maximal* signal that may be associated with S in the (noisy) spectra. Relative errors are 50%.

[2] S/W ratio is calculated by assuming (1) no loss of F atoms (namely 17 per molecule) and (2) by averaging over the sample thickness. Uncertainty of ±15% (relative error) should be considered due to variations in the flake thickness.

Analysis of WSe₂ oxidation by XPS:

For the compositional analysis, the Si-oxide layer, on top of which WSe_2 crystals were deposited, introduced technical difficulties. The study of oxidation defects of the WSe_2 plates could hardly gain from the analysis of O signals and, therefore, was based on the W and Se lines only. Detailed XPS spectra for the W 4f and Se 3d are given in **Supplementary Figure 1**, showing the oxidation of these elements in the bare sample; oxidation that disappears after the deposition of thiol molecules.
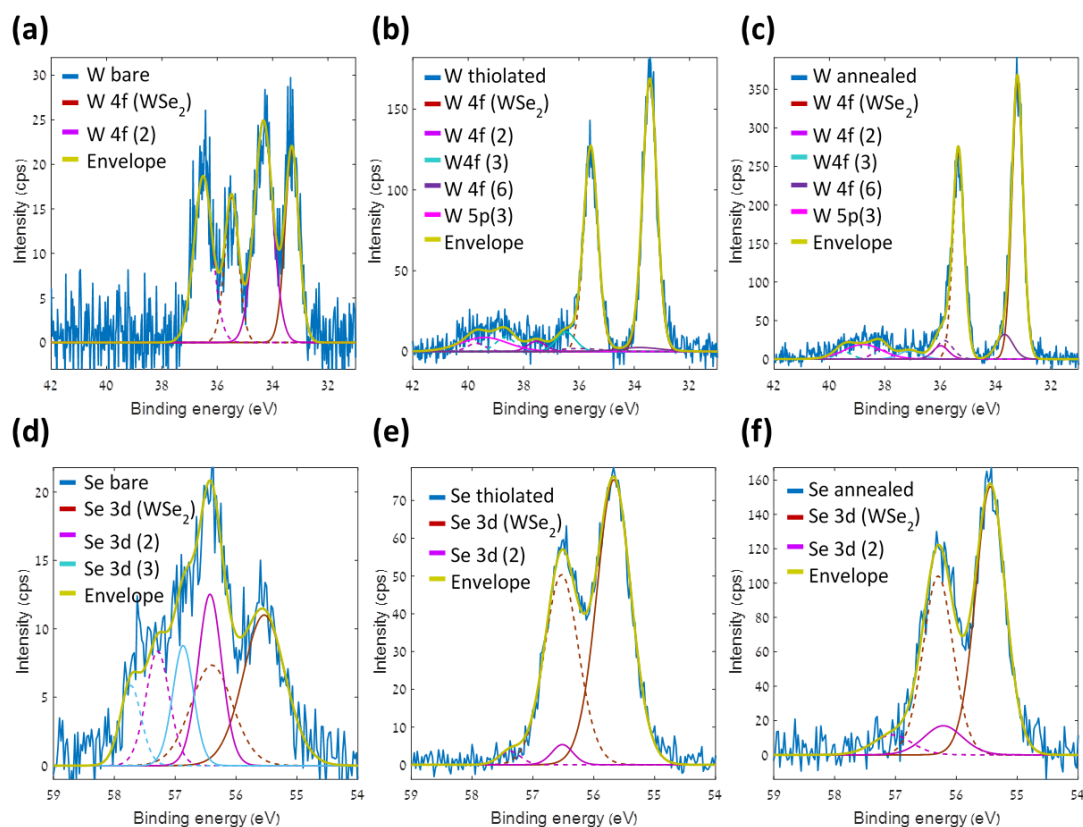
Supplementary Figure 1. XPS spectra of the WSe_2 single layer, where the (a-c) W 4f and (d-f) Se 3d oxidation states can be identified: (a) and (d) bare samples; (b) and (e) thiolated; (c) and (f) annealed. Each W spectrum consists of dominant 4f doublets, with energy split of 2.18 eV in each, plus much weaker 5p signals at corresponding chemical shifts. The Se 3d spectrum consists of doublets with energy split of 0.86 eV in each. Note the pronounced oxide signals, W^{ox} (attributed to WO_3) and Se^{ox} (due to varied oxidation states of Se), in the bare samples. After thiolation and, even more, after annealing, these oxide signals are suppressed, whereas the W^{Se} and Se^W lines become more pronounced, indicating removal of defects. The broad Se 3d line in (d) indicates partial oxidation of Se in the sample with, at least, two oxidation states of Se, besides the $MoSe_2$ state.

Attempting detailed quantification of the curing steps, we could not gain much from the carbon signal, because it was dominated by a seeding promoter layer that appeared in all cases on open areas of the silica. Yet, a rough indication is seen in Table 1, where the total amount of carbon increases upon thiol adsorption and decreases, as expected, after annealing and 'burning' the alkane chains.

Calculation of the effective molecular layer thickness on the surface:

Our estimations of coverage by molecules are based on standard photoelectron attenuation models. We assume the attenuation length parameter to have a common, average value for the various electron energies relevant here, taking $\lambda_1 = 2.5$ nm for the dichalcogenide medium and $\lambda = 3.3$ nm for the organic medium. Next, we denote an average crystal thickness, D, found to be around four molecular layers for the samples with fluorinated molecules, namely $D_{WSe2} = 2.5$ nm. It should be noted that D was much smaller in most of the samples, down to a single molecular layer.

Based on standard photoelectron attenuation models, the intensity ratio of the molecules/ WSe_2 substrate can be expressed as:

$$\frac{I_{molecules}}{I_{WSe_2}} = R = \frac{1 - e^{-d/\lambda}}{e^{-d/\lambda}(1 - e^{-D/\lambda 1})} = \frac{e^{d/\lambda} - 1}{1 - e^{-1}} \tag{1}$$

where d is an effective thickness of the molecular layer, to be extracted hereafter, and on the left side of the equation we use the measured XPS intensities.

For the total intensity of the over layer we cannot use the C signal, but instead rely on the S or F signals.

Specifically for the fluorinated molecules we use: $I_{molecules} = \frac{27}{17} * I_F$

(because 17 fluorine atoms represent 27 atoms in total in a PFDT chain).

Similarly, the intensity of the WSe_2 substrate is taken as: $I_{WSe_2} = 3 * I_W$

where I_W is the reduced component only in the W 4f spectrum and a check for consistency with the Se signal is made in all cases. Thus, the layer thickness can be estimated from the measured ratio of $\frac{I_F}{I_W}$ as follows:

$$\frac{I_{molecules}}{I_{WSe_2}} = R = \frac{27/17 * \frac{I_F}{I_W}}{3} \tag{2}$$

Which translates to the d-values given in the text.

Time-dependent XPS spectra:

In this section, additional explanation is provided for the unusual result observed at the bare samples. To start with, the sample current (recorded on its back contact) is definitely positive in all cases (which means that integrally the sample loses electrons).

The sample is grounded at its substrate bottom side, hence standard electrostatic modeling of a planar system would dictate the changes in surface potential to be given

by a weighted summation over sheet charge densities, σ_i, according to their vertical location, z_i, namely $\Sigma z_i \sigma_i$. Thus, a minor amount of top surface charge can, in principle, dominate the local potential and, in particular, dictate a negative sign even if the total amount of captured charge is positive. A dedicated explanation of these effects will be given elsewhere [in preparation].

Supplementary Figure 2 shows the raw time dependence of line shifts, evaluated for representative components in the XPS data. While the thiolated and annealed samples (red and green curves, respectively) show 'normal' behavior, namely negligible or clear positive charging, the bare sample signals (blue) reflect negative charging like shifts. Importantly, the W shifts in the latter are larger in magnitude than those of the oxygen and Si. Therefore, considering the above arguments, we interpret this result as accumulation of trapped electrons at top surface sites (hence, the dichalcogenide flakes), whereas positive charge does accumulate in the Si-oxide layer.
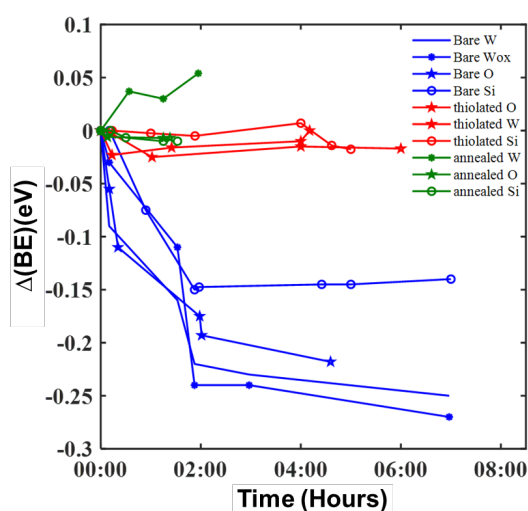

Supplementary Figure 2. Binding-energy shifts, $\Delta(BE)$ of W^{Se}, W^{ox}, Si and O lines, as a function of exposure time to the x-ray source. The shifts for the bare sample (blue) are in opposite direction to those of the thiolated (red) and annealed (green) samples.

Detection of sulfur by ToF-SIMS:

The direct measurement of sulfur by means of mass spectra may be impaired by the proximity of sulfur mass fraction so that of O_2 signal (O_2 = 31.998 amu, S = 32.066 amu) emitted from the substrate. In the same way WS_2^- signal can be attributed to WO_4^-. Still, ToF-SIMS measurement can detect S on the aggregate coverage areas as a

relative measurement between the uncoated (bar) and coated (annealed) samples (**Supplementary Figure 3**).
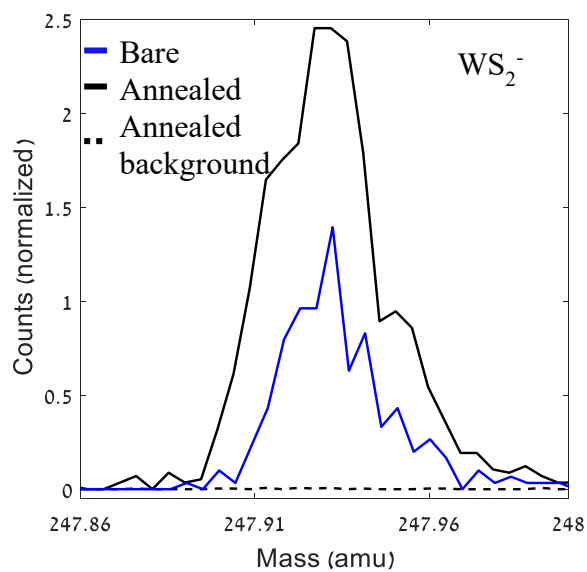
Supplementary Figure 3. TOF-SIMS spectra WS_2^- mass fraction collected from the bare sample (blue line), annealed sample (black line) and from the SiO_2 substrate background (black dash).

Supplementary Note II: Gate-Modulated Photoluminescence

Gate-Modulated Photoluminescence

Measuring the gated PL signal of WSe_2 FET devices revealed a hysteresis effect in the intensity, width, and energy values (**Figure 3a-c**, respectively). Long duration measurements showed that a gate voltage step triggers a sharp transient in the PL signal which decays over hundreds of seconds (**Supplementary Figure 4**). The long lifetimes were indicative that defect states are responsible[1–3].
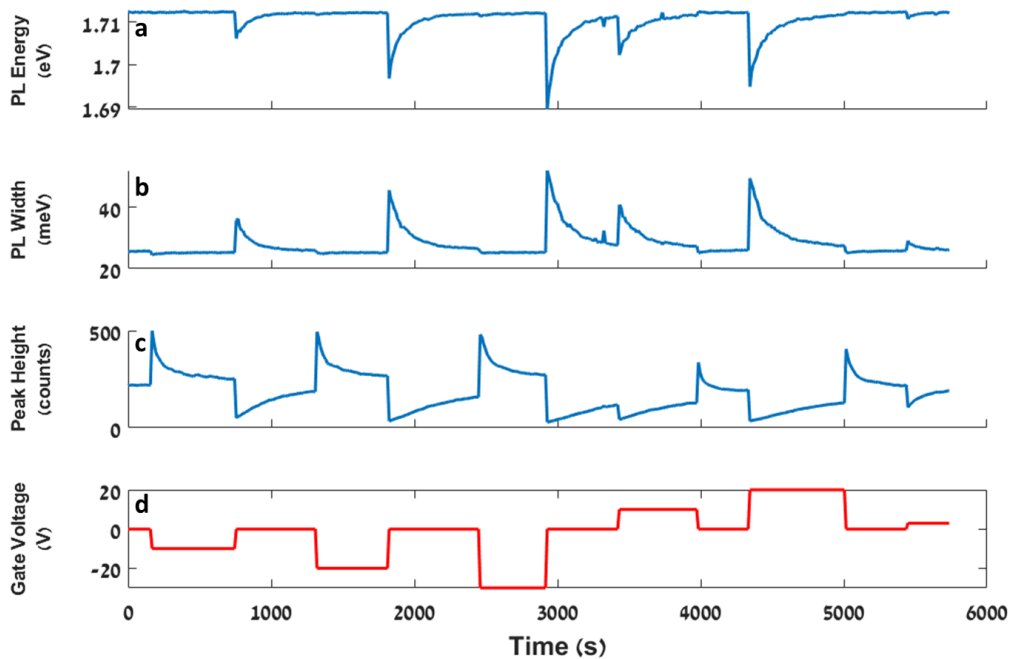
Supplementary Figure S4. PL behavior over time with changing gate voltage. (a) PL energy. (b) Peak width. (c) PL intensity. (d) Gate Voltage V_g.

For negative voltage steps (positive charging of device) there is little to no effect on the spectral width and peak energy, and a sharp enhancement in PL intensity is observed. Adding a thin hBN layer as a buffer between the WSe_2 and the SiO_2 substrate eliminates this enhancement (not shown), suggesting that it stems from interaction with surface defects related to the oxide layer. For positive voltage steps (negative charging), a transient can be observed in all three parameters: The PL peak is red-shifted and spectrally broadened, and the PL intensity is quenched. The transient's form over time, starting at the gate voltage step at $t = 0$, is that of a decaying exponent function (**Figure 3d-f**):
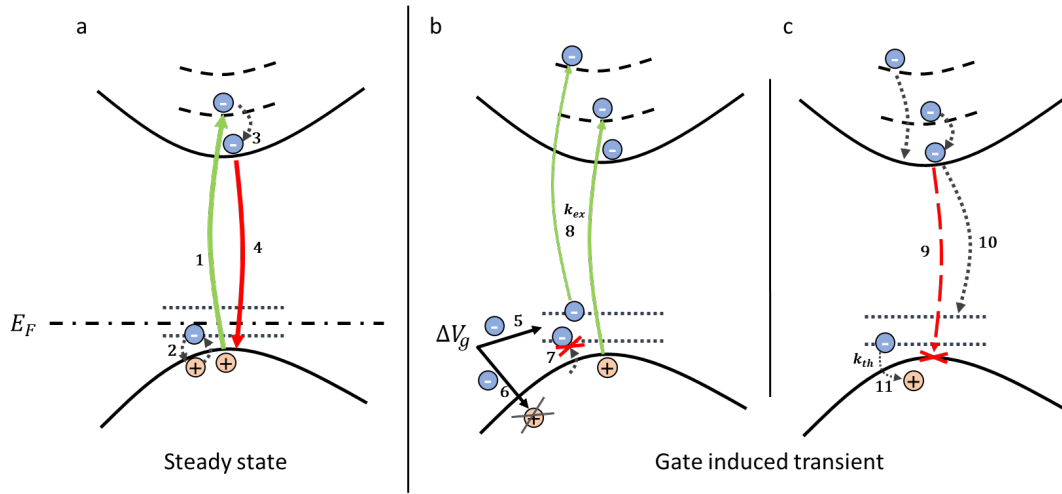
$$E = E_0 + \Delta E e^{-k_E t} \tag{3}$$

$$w = w_0 + \Delta w e^{-k_w t} \tag{4}$$

$$I = I_0 + \Delta I e^{-k_I t} \tag{5}$$

This corresponds to a steady state PL signal with intensity I_0, spectral width w_0, and peak energy E_0, with a transient modulation proportional to the density of charged defect states, which exponentially decays over time.


Supplementary Figure 5 - Schematic diagram of the processes occurring during a PL measurement. During the steady-state (a), holes are generated in the valence band via photo-excitation (1) and thermal excitation into defect states (2). Photoexcited electrons undergo thermal relaxation (3), and photo-recombination (4), emitting a photon in the process. The gate induced transient state is described in two panels (b, c) for clarity purposes. The gate voltage step traps electrons in defect states (5). The injected electrons also annihilate photo and thermally generated holes in the valence band (6). The charged defect states prevent thermal generation through Pauli blocking (7). Finally, photo-excitation occurs from both the valence and defect states (8). These all reduce the ratio of available photo-recombination paths, which reduces photorecombination (9), and increases transitions into defect states (10), the majority of which are non-radiative. This red-shifts and quenches the PL signal. Electrons gradually escape via thermal relaxation (11) with rate k_{th} and the photoexcitation (8) with rate k_{ex} which return the device to the steady state.

Supplementary Figure 5 schematically describes the process responsible for the observed PL transient. Field effect induced electrons are trapped in defect states. These trapped electrons cause a PL broadening as result of the disorder and due to radiative transitions from the conduction band edge to unoccupied defect states. The observed quenching and spectral red-shift are caused by several factors: (i) The field effect charging of the defect levels prevents thermal generation from the valence band into the occupied traps through Pauli blocking. (ii) The field effect induced electrons annihilate photogenerated holes directly. (iii) Photoexcitation occurs from both valence and defect levels. These factors all reduce the ratio of available photorecombination

paths, resulting in a red-shifted and quenched PL peak. The correlation between charge density injected by field effect and the resulting PL quenching was utilized for evaluating the density of defect states in the samples (see **Table 1** in the main text).

Gradual discharge of the defect states returns the PL signal to the original steady state regardless of the applied modulation amplitude of the gate voltage. There are two mechanisms in which the trapped electrons can escape: photoexcitation[4] with a mean lifetime τ_{ex}, and thermal relaxation with a mean lifetime of τ_{th}. Their respective rates are defined as $k_{ex} = \tau_{ex}^{-1}$ and $k_{th} = \tau_{th}^{-1}$.

The total escape rate k is a linear combination of the k_{ex} and k_{th}. To evaluate the contribution of each factor, an illumination duty cycle was used to control the average excitation intensity (**Supplementary Figure 6a**).
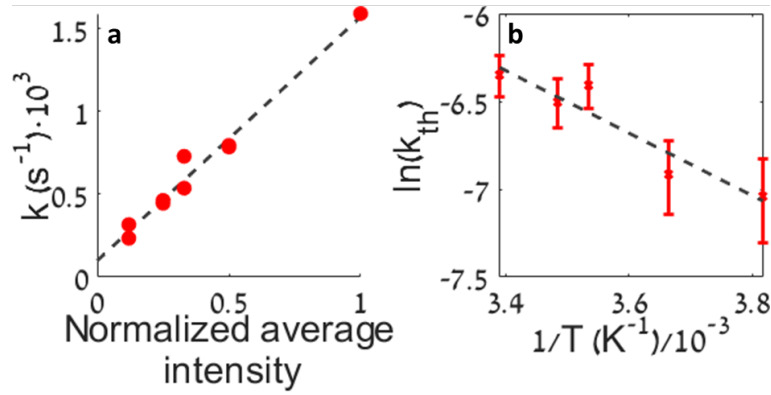
Supplementary Figure 6- the relaxation constant **k** as a function of average illumination intensity (a). The thermal relaxation constant as a function of inverse temperature (b). The error bars of (b) indicate the range of values of k_{th} corresponding to the range of values of k_{ex} as depicted from the confidence interval of the linear fit in (a).

The slope $k_{ex} = 1.47 \cdot 10^{-3} \pm 2.1 \cdot 10^{-4} s^{-1}$ is the photoexcitation-induced escape rate at full illumination intensity. The intercept corresponds to the escape rate in absence of light, *i.e.*, it is the thermal relaxation rate at room temperature $k_{th}(295K) = 9.9 \cdot 10^{-5} \pm 9.5 \cdot 10^{-5} s^{-1}$.

Additionally, $\frac{k_{ex}}{k_{ex}+k_{th}} = 0.94$ $\frac{k_{th}}{k_{ex}+k_{th}} = 0.062$ *i.e.*, under our illumination conditions ~94% of the escaped electrons are due to photonic excitation, and ~6% due to thermal relaxation.

To find the effect of temperature on the thermal relaxation rate $k_{th}(T)$, the photoexcitation rate k_{ex} was assumed to be constant. Therefore, the value of k_{ex} measured at room temperature may be subtracted from k to obtain k_{th}. We assume that defect states' binding energy acts as an activation barrier, and therefore k_{th} is described by the Arrhenius relation as:

$$k_{th} = k - k_{ex} = Ae^{-\frac{E_a}{k_B T}} \tag{6}$$

The thermal rate k_{th} is deduced by subtracting the known value for k_{ex} from k. It is compared to the Arrhenius equation on the right-hand side, where A is a constant, E_a is the activation energy, k_B is the Boltzmann constant, and T is the absolute temperature.

Taking the natural logarithm of both sides of (6) yields the linear dependence :

$$ln(k_{th}) = -\frac{E_a}{k_B} \cdot T^{-1} + ln\,(A) \tag{7}$$

The linear relation (7) relates the thermal rate k_{th} to the inverse temperature T^{-1}, where A is a constant, E_a is the activation energy, k_B is the Boltzmann constant.

Supplementary Figure 6b shows the thermal relaxation rate k_{th} *vs.* temperature according to (7). The error bars indicate the range of values of k_{th} corresponding to the range of values of k_{ex}. The crosses indicate the most probable value, and the dashed line indicates the best linear fit. The linear fit shows that the thermal release is well described by an activation barrier, with $\boldsymbol{E_a = 153 \pm 97 meV}$.

The steady state PL intensity increases with temperature (**Supplementary Figure 7a**) due to increased thermal generation, as well as an increased probability of indirect transitions. The PL quenching factor Q is defined to be the relative loss of PL intensity at $t = 0$ (when a gate voltage step occurs): $Q \equiv -\frac{\Delta I}{I_0}$, where $I = I_0 + \Delta I e^{-k_I t}$ describes the PL intensity transient as a function of time. The quenching factor increases with temperature (**Supplementary Figure 7b**), *i.e.,* more intensity is lost at $t = 0$, due to a larger existing fraction of thermally generated recombination sites, which are subsequently blocked by the field effect injected charges at the gate voltage step.
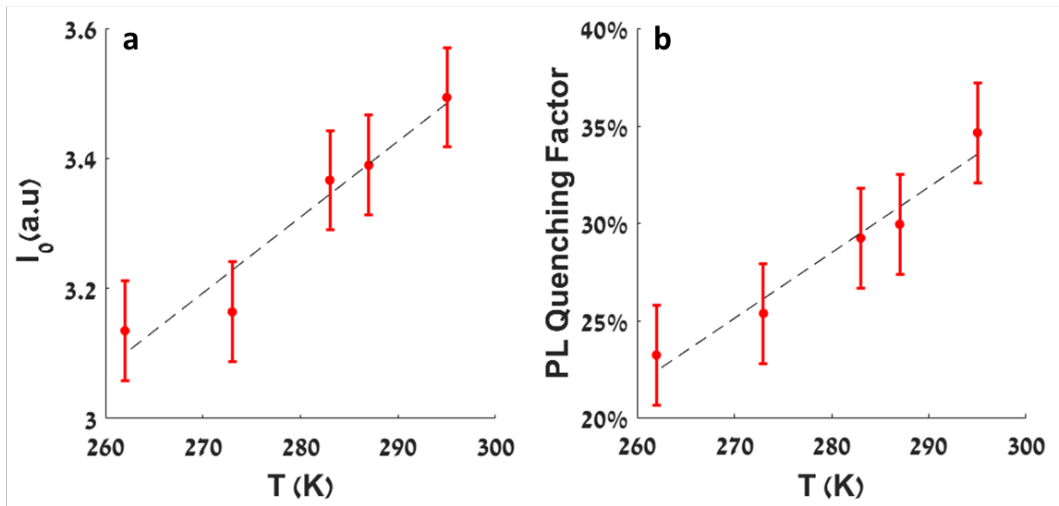
Supplementary Figure 7. Voltage-mediated PL intensity (a) and quenching factor (b) vs. temperature. The error bars correspond to confidence intervals used when fitting measured dependence of PL intensity in time, according to equation (5).

References

1.   Jiang, J. *et al.* Defect Engineering for Modulating the Trap States in 2D Photoconductors. *Advanced Materials* **30**, 1804332 (2018).

2.   Han, P. *et al.* Ambient Effects on Photogating in MoS 2 Photodetectors.

3.   Kriegel, I. *et al.* Contactless photo-induced carrier density control in nanocrystal MoS 2 hybrids.

4.   Yin, L. *et al.* Robust trap effect in transition metal dichalcogenides for advanced multifunctional devices. *Nature Communications 2019 10:1* **10**, 1–8 (2019).